Gravitational Waves from a Core g Mode in Supernovae as Probes of the High-Density Equation of State

Pia Jakobus[®], * Bernhard Müller[®], and Alexander Heger[®] School of Physics and Astronomy, Monash University, Clayton, VIC 3800, Australia

Shuai Zhao

Yunnan Observatories, Chinese Academy of Sciences (CAS), Kunming 650216, China; Key Laboratory for the Structure and Evolution of Celestial Objects, CAS, Kunming 650216, China; and International Centre of Supernovae, Yunnan Key Laboratory, Kunming 650216, China

Jade Powell

Centre for Astrophysics and Supercomputing, Swinburne University of Technology, Hawthorn, VIC 3122, Australia

Anton Motornenko, Jan Steinheimer[®], and Horst Stöcker[®] Frankfurt Institute for Advanced Studies, Giersch Science Center, Frankfurt am Main, Germany

(Received 16 January 2023; revised 18 April 2023; accepted 29 September 2023; published 7 November 2023)

Using relativistic supernova simulations of massive progenitor stars with a quark-hadron equation of state (EOS) and a purely hadronic EOS, we identify a distinctive feature in the gravitational-wave signal that originates from a buoyancy-driven mode (g mode) below the proto-neutron star convection zone. The mode frequency lies in the range $200 \lesssim f \lesssim 800$ Hz and decreases with time. As the mode lives in the core of the proto-neutron star, its frequency and power are highly sensitive to the EOS, in particular the sound speed around twice saturation density.

DOI: 10.1103/PhysRevLett.131.191201

Introduction.—Core-collapse supernovae are among the most important astronomical events vet to be detected by ground-based gravitational-wave (GW) interferometers [1–5]. With current detector sensitivity, the event must occur within at most a few 10 kpc of Earth [4,6,7]. Future detectors, such as the Einstein Telescope, may observe supernovae throughout the Milky Way and beyond the Magellanic Clouds [8-11]. The estimated rate for galactic core-collapse supernovae (CCSNe) is $3^{+7.3}_{-2.6}$ per century [12,13], implying a realistic chance of detection within the lifetime of second- and third-generation instruments. Such a detection would reveal insights into the properties of the proto-neutron star and the multidimensional fluid flow in the supernova core. Multidimensional simulations [e.g., [14–25]] show that the GW signal reflects the presence of proto-neutron star (PNS) oscillation modes triggered by convection, turbulent accretion, the standing-accretion shock instability [26], or triaxial instabilities. The most robust feature in the signal comes from a quadrupolar f/qmode [15,21,27–31] with a frequency that increases in time from a few hundred Hz to above 1 kHz. Future GW observations may measure this frequency [32,33] and use mode relations [15,34,35] to constrain bulk PNS parameters (mass, radius, surface temperature).

Unfortunately, the dominant f/g mode is largely confined to the PNS surface region and therefore only indirectly sensitive (through the PNS radius) to the

high-density equation of state (EOS). Nevertheless, potential GW diagnostics that could also constrain the properties of nuclear matter at several times nuclear saturation density $\rho_0 \geq 2.6 \times 10^{14} \ \mathrm{g \ cm^{-3}}$ and temperatures of several 10 GK are being identified. The GW signal could shed light on the nuclear EOS, e.g., about the possible appearance of quarks at high densities [36,37], which is not considered in most standard core-collapse supernova simulations (CCSNe). A first-order phase transition from hadrons to quarks [38,39], which is already known to strongly affect postmerger GW emission in neutron star mergers [40–43], produces a loud and distinct supernova GW signature with a peak at several kHz, regardless of whether the phase transition triggers an explosion [44–46].

Here, we compare the predicted GW signals from supernova simulations with the purely hadronic SFHX EOS [47] and the chiral mean-field (CMF) EOS [48] with a *smooth crossover* to quark matter. We find that the CMF models exhibit a *core g*-mode signature of lower frequency and higher intensity as a distinct GW fingerprint, and elucidate the underlying EOS properties.

Methods.—We perform axisymetric (2D) simulations with the general-relativistic neutrino hydrodynamics code CoCoNut-FMT [49,50]. Different from recent multi-D simulations with CoCoNut-FMT, we calculate only a small inner region of radius < 1380 m in spherical symmetry to capture g modes in the PNS core. GW signals are calculated using a

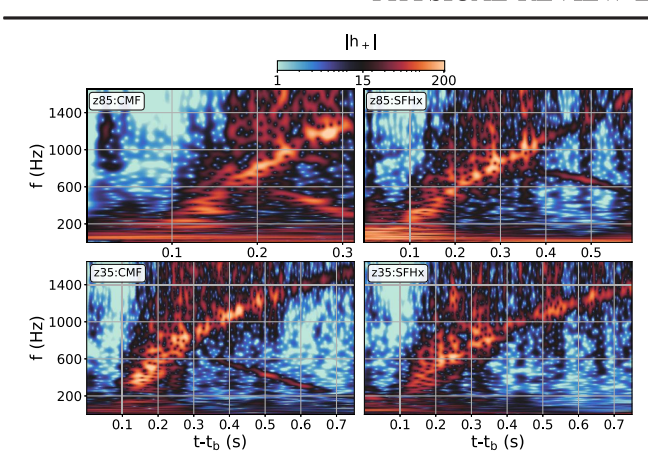


FIG. 1. GW spectrograms for z85 (top) and z35 (bottom) using the CMF EOS (left) and SFHx EOS (right). The same logarithmic color scale for the amplitude $|h^+|$ is used for all models. Models z85:CMF, z85:SFHx, and z35:CMF exhibit a distinct second frequency band from the 2g_1 mode, which branches off the dominant band after a few hundred milliseconds.

modified version [15] of the time-integrated quadrupole formula [51]. We use two zero-metallicity progenitors of $35M_{\odot}$ and $85M_{\odot}$ (named z35 and z85), which are calculated with the stellar evolution code KEPLER [52,53].

We employ two different high-density EOS. For models z35:CMF and z85:CMF, we use the CMF model with a firstorder nuclear liquid-vapor phase transition at densities $\sim \rho_0$, a second but weak first-order phase transition due to chiral symmetry restoration at $\sim 4 \times \rho_0$ with a critical endpoint at $T_{\rm CeP} \approx 15$ MeV, and a smooth transition to quark matter at higher densities. The CMF EOS has a ground state density (for symmetric matter) $n_{\rm sat} = 0.16 \; {\rm fm}^{-3}$, binding energy per baryon $E_0/B = -15.2$ MeV, asymmetry energy $S_0 = 31.9$ MeV, incompressibility $K_0 = 267$ MeV, and a maximum Tolman-Oppenheimer-Volkoff mass $M_{
m TOV}^{
m max}=$ $2.10M_{\odot}$ [48]. This EOS has recently been studied in the context of neutron star merger and 1D core-collapse supernova simulations [54,55]. The second EOS, used for runs z35:SFHx and z85:SFHx, is the purely hadronic relativistic mean-field SFHx model [47]. Nuclear matter properties for the SFHx EOS are $n_{\text{sat}} = 0.16 \,\text{fm}^{-3}$, $E_0/B = -16.16 \,\text{MeV}$, $S_0 = 28.67 \text{ MeV}, K_0 = 239 \text{ MeV}, \text{ and } M_{\text{TOV}}^{\text{max}} = 2.13 M_{\odot}.$

Results.—Dynamically, the CMF and SFHx models exhibit similar behavior. Both z85 models undergo shock revival followed by early black hole (BH) formation, albeit earlier by more than 0.2 s in z85:CMF. Both z35 models explode. The GW signals of the CMF and SFHx models exhibit distinctive differences, however. Figure 1 shows GW spectrograms computed using the Morlet wavelet transform [56].

The early phase of GW emission is still similar for both EOS. The z85 models show low-frequency emission at \sim 100 Hz due to prompt convection and early standing-accretion shock instability activity [14,15,57,58]; this is

largely absent in the z35 models. Subsequently, the PNS surface f/g mode [15,21,28,29] appears as a prominent emission band with frequencies that increase from ~300 Hz to above 1000 Hz. The f- or g-mode frequency rises slightly faster in the CMF models.

The most striking differences are found in another emission band of *decreasing* frequency that branches off the dominant f/g mode between 0.2 s and 0.35 s, except in z35: SFHx, which shows no such signal. A linear mode analysis (see Refs. [21,29,30,35] for the methodology) identifies this frequency band as the decreasing branch of the 2g_1 mode (Zha *et al.* in prep.), i.e., a quadrupolar g mode with one node, with an eigenfunction mostly confined to the PNS core (core g mode). Henceforth, we refer to the decreasing branch as the 2g_1 mode for short. (The dominant band with increasing frequency follows the *increasing* branch of the 2g_1 mode initially and then the f mode after the avoided crossing of the two modes. The mode classification is, e.g., sensitive to the boundary condition in the linear analysis).

The mode frequency f_{2g_1} is systematically lower in z85: CMF compared to z85:SFHx. In z85:CMF, f_{2g_1} decreases from ~600 Hz at 0.2 s to ~220 Hz at 0.32 s, at which point the model collapses to a BH. In z85:SFHx, black-hole collapse occurs later and f_{2g_1} evolves more slowly from a higher frequency of ~800 Hz down to ~560 Hz at 0.58 s. In z35:CMF, the 2g_1 mode lives at similarly low frequencies as in z85:CMF, i.e., in the range 220–600 Hz.

Such pronounced emission in the declining 2g_1 mode frequency band as in the CMF models (and to a lesser extent model z85:SFHx) is not usually observed in simulations with energy-dependent neutrino transport. These usually show an emission gap at the avoided crossing with the f mode [21]. The 2g_1 mode has been found in simulations with more approximate neutrino transport [59,60], or modified Newtonian gravity [25,29,34].

To further confirm the nature of the mode, we perform a spatially resolved Fourier analysis of the integrand of the quadrupole formula using high-time-resolution simulation output with sampling frequency 10^4 Hz. To detect quadrupolar motions as a function of radius and frequency, we integrate over angle only, and obtain a radius-dependent measure q(r,t) of quadrupolar perturbations,

$$q(r,t) = \frac{32\pi^{3/2}G}{\sqrt{15}c^4} \int_0^{\pi} d\theta \, \phi^6 r^3 \sin\theta \times \left\{ \frac{\partial}{\partial t} \left(S_r (3\cos^2\theta - 1) \right) + \frac{3}{r} S_\theta \sin\theta \cos\theta \right\}.$$
 (1)

 ϕ is the conformal factor of the space-time metric, and S_r and S_{θ} are the orthonormal components of the relativistic momentum density.

We obtain spectrograms of q(r,t) (Fig. 2, first two panels) using the fast Fourier transforms in a fixed time window Δt and apply additional denoising by convolving

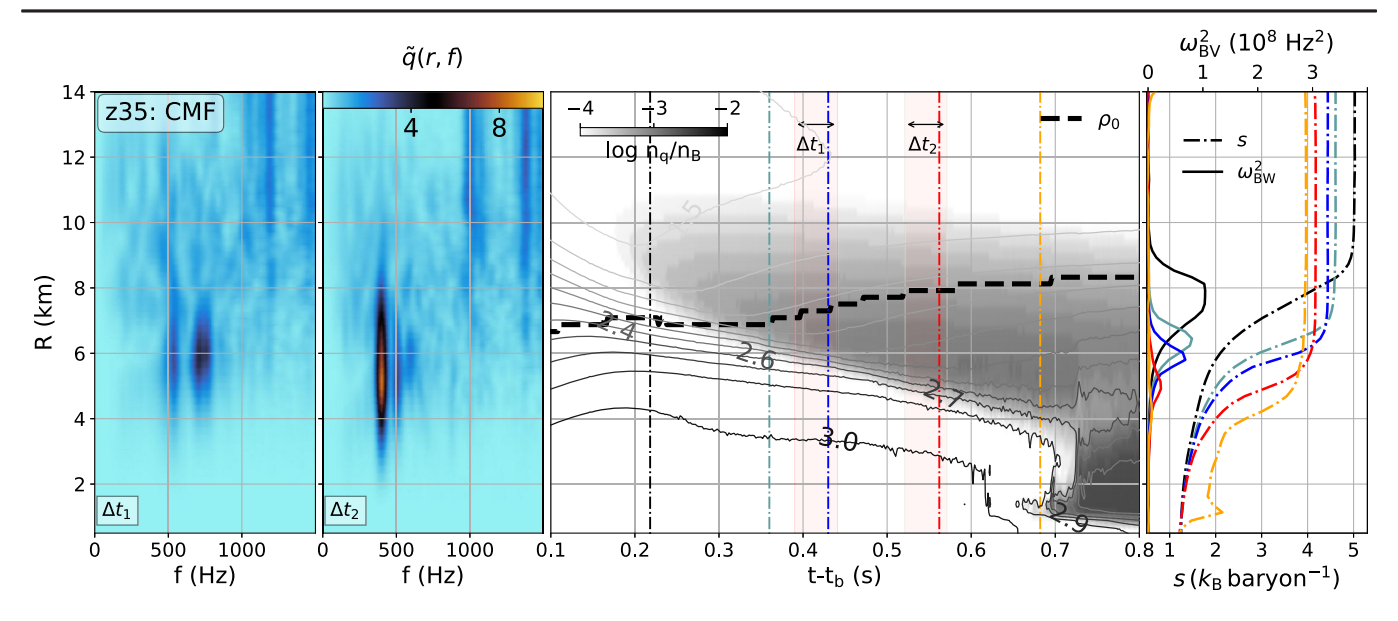


FIG. 2. First and second panels: amplitude $\tilde{q}(r,f)$ of the Fourier transform of the quadrupolar perturbation q(r,t) as a function of radius and frequency f for the time intervals Δt_1 and Δt_2 around 0.4 s and 0.55 s (indicated in red shades in the third panel) for model z35:CMF. Third panel: color contour plot of the quark fraction n_q/n_B as a function of time and radius, combined with isocontours for the adiabatic index (solid lines in different shades of gray) and a thick black line indicating the radius corresponding to nuclear saturation density. Fourth panel: Brunt-Väisälä frequency $\omega_{\rm BV}^2$ (solid lines) and spherically averaged specific entropy per baryon s, (dashed) at five different times, which are indicated on the time axis of the third panel as vertical lines of the respective color. The last entropy profile (orange) shows a blip at a radius of less than 2 km, which is due to a convective plume that penetrates the PNS core when the buoyancy barrier at the inner edge of the PNS convection zone is eroded ($\omega_{\rm BV}^2 \approx 0$).

the fast Fourier transforms with a weighted sum of radial basis functions [61].

Spectrograms are shown for two time windows Δt_1 and Δt_2 around 0.4 s and 0.55 s (marked as red shaded areas in the third panel of Fig. 2) for model z35:CMF. During Δt_1 , the spectrograms show power corresponding to the lowfrequency signal 4 km $\lesssim r \lesssim 8$ km and a frequency of ~600 Hz, with a weaker "hot spot" at ~500 Hz. Later, during Δt_2 , the hot spot is stronger and its centroid shifts towards small radii (although it still reaches out to ~8 km) as the PNS contracts. The frequency decreases to ~430 Hz and is clearly defined. Profiles of the relativistic Brunt-Väisälä frequency $\omega_{\rm BV}^2$ [15] and specific entropy per baryon s (Fig. 2, fourth panel) show that the mode is located at the *inner* boundary of the PNS convection zone, originating from a different region than the high-frequency emission, which is visible in two streaks above 1 kHz at larger radii. The profiles of $\omega_{\rm BV}^2$ also explain the downward trend in frequency as the peak in $\omega_{\rm BV}^2$ decreases with time. All of this strongly supports the identification as a core

This still leaves the question why the 2g_1 mode has a significantly lower frequency and is more strongly excited in the CMF models. Before a more quantitative analysis, it is important to note that quark formation is not *directly* responsible in the CMF models for the smaller mode frequency as evident from the time- and radius-dependent quark fraction $n_q/n_{\rm B}$ (Fig. 2, third panel).

Although quarks appear off-center at 8 km $\lesssim r \lesssim 10$ km quite early at ~ 0.2 s, they appear only in small numbers $n_q/n_{\rm B} \leq 10^{-4}$. The appearance of quarks at low densities is due to the absence of a sharp phase transition in the CMF EOS and the high temperatures in the PNS mantle, but is of little dynamical relevance. Quarks only appear more abundantly and lead to significant softening later at ~ 0.7 s at radii ~ 2 km. Thus, the full transition to quark matter comes too late to account for the distinct 2g_1 mode in z35:CMF as opposed to z35:SFHx well before 0.7 s.

The lower 2g_1 mode frequency in the CMF models is rather connected to lower peaks of $\omega_{\rm BV}^2$ at the inner boundary of the PNS convection zone at densities below $2\times \rho_0$ (colored solid lines in Fig. 3). At late times the buoyancy barrier at the bottom of the PNS convective zone disappears almost entirely, and the entropy profiles show overshooting into the core as favorable conditions for "inverted convection" to develop [55]. The reason for the lower Brunt-Väisälä frequency can be analyzed by writing $\omega_{\rm BV}^2$ as

$$\omega_{\rm BV}^2 = \frac{\mathrm{d}\alpha}{\mathrm{d}r} \frac{\alpha}{\rho h \phi^4} \frac{1}{c_s^2} \left[\left(\frac{\partial P}{\partial s} \right)_{\tilde{\rho}, Y_{\rm e}} \frac{\mathrm{d}s}{\mathrm{d}r} + \left(\frac{\partial P}{\partial Y_e} \right)_{\tilde{\rho}, s} \frac{\mathrm{d}Y_{\rm e}}{\mathrm{d}r} \right], \quad (2)$$

and considering the impact of the various gradients and thermodynamic derivatives. Here, α is the lapse function, ρ is the baryonic mass density, $\tilde{\rho}$ is the total mass-energy

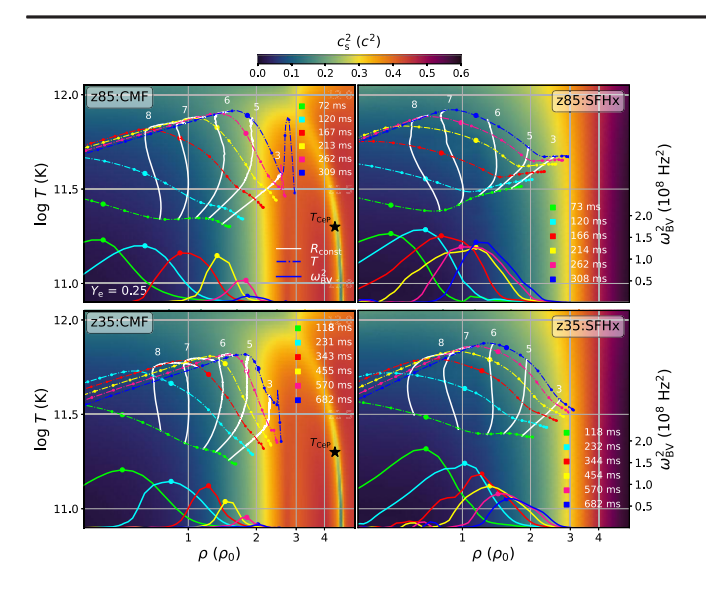


FIG. 3. Color contour plots of the squared sound speed c_s^2 as a function of density ρ and temperature T for an electron fraction of $Y_e=0.25$ for models z85 (top) and z35 (bottom) with the CMF EOS (left), and the SFHx EOS (right). Solid and dashed curves show $\omega_{\rm BV}^2$ and (spherically averaged) temperature profiles $T(\rho)$ at various times (indicated by line color). The density where $\omega_{\rm BV}^2$ peaks is indicated by a dot on the curves. The white lines indicate five constant radii; the radius (in km) is indicated on top. Note a temperature blip at high densities due to the overshooting of plumes into the PNS at late times (blue curves) in the CMF models.

density, P is the pressure, $h = (\tilde{\rho} + P/c^2)/\rho$ is the relativistic enthalpy, Y_e is the electron fraction, and c_s is the sound speed. The most conspicuous feature in the CMF models is a higher sound speed than in the SFHx models at the location corresponding to the maximum of $\omega_{\rm BV}$ (color shading in Fig. 3), once the inner edge of the PNS convection zone contracts to densities of about $2 \times \rho_0$. This is due to significant stiffening of the CMF EOS owing to baryon-baryon repulsion [48]. Although not directly related to the formation of quark matter, such pronounced stiffening at moderately high densities is characteristic of currently viable EOS with a phase transition or crossover to quark matter [62–64]. The stiffening is crucial for achieving maximum neutron star masses compatible with observational constraints and tentatively supported by heavy-ion collisions [65,66]. On top of the systematic difference in sound speed between the two EOS, we also find a somewhat disparate PNS structure, which complicates the comparison of $\omega_{\rm RV}^2$ between CMF and SFHx models, e.g., the inner edge of the PNS convection zone as defined by the peak in ω_{BV} tends to lie at higher densities in the CMF models. Although the difference in sound speed has a clear impact on $\omega_{\rm BV}$ and can be readily connected to the underlying physics of the EOS, there are further smaller effects that will eventually need to be incorporated in a rigorous theory for the EOSdependence of the 2g_1 mode. Differences in the electron fraction gradient dY_e/dr also contribute to the lower $\omega_{\rm BV}$ for CMF. Different from the SFHx models, dY_e/dr becomes negative in the region of interest before the onset of the signal. With positive $(\partial P/\partial Y_e)_{\tilde{\rho},s}$, the second term in brackets in Eq. (2) then decreases $\omega_{\rm BV}$, especially since $(\partial P/\partial Y_e)_{\tilde{\rho},s}$ diverges from the SFHx EOS at this point and becomes larger by up to a factor of 4 in the PNS core in the CMF models. The ultimate cause for the different behavior is that the small "hump" in Y_e at a mass coordinate of $\sim 0.7 M_{\odot}$ that is imprinted on the PNS structure shortly after bounce is erased quicker by neutrino diffusion in the CMF models. The terms $(\partial P/\partial s)_{Y_e,\tilde{\rho}}$ and ds/dr also show some EOS dependence, but their net effect is even smaller. Details are shown in the Supplemental Material [67].

It is more challenging to trace the higher *power* in GWs emitted by the ${}^{2}g_{1}$ mode to the PNS structure and to EoS properties. Stronger excitation of the 2g_1 mode in the CMF models could be due to stronger PNS convection or more efficient coupling between the forcing convective motions and the 2g_1 mode. Stronger convection in the CMF models appears to at least play an important role. The turbulent kinetic energy in the PNS convection zone is about an order of magnitude larger in z35:CMF at several 10⁵⁰ erg than in z35:SFHx, and still somewhat larger in z85:CMF than in z85:SFHx (see Supplemental Material). Both z85 models have significantly higher turbulent convective energies than the z35 models in line with recent findings of stronger PNS convection for more massive progenitors [68]. The higher convective energies are mostly due to higher turbulent velocities and less due to differences in the mass of the PNS convection zone. The empirical finding of stronger PNS convection in the CMF models explains the conspicuous signal from the ${}^{2}g_{1}$ mode in the GW spectrograms, but further work is needed to identify the underlying physical reason. Unfortunately, the dynamics of PNS convection are not fully understood because of the complicated interplay of stabilizing and destabilizing stratification gradients and multidimensional convective flow [e.g., [10,69–72]]. It is noteworthy, however, that a significant impact of EOS properties on the long-term behavior of PNS convection during the Kelvin-Helmholtz cooling phase has been reported before [73].

Conclusions.—Our 2D supernova simulations with a quark-hadron CMF EOS [48] and the hadronic SFHx EOS [47] show a characteristic GW emission band with decreasing frequencies of several hundred Hz in addition to the well-known emission band from the dominant f/g mode. We identified a core g mode (2g_1 mode) that mostly lives around the inner boundary of the PNS convection zone as the oscillation mode responsible for this GW feature.

The mode frequency and power are very sensitive to the high-density EOS. For a $35M_{\odot}$ progenitor, the GW signal from the 2g_1 mode is only present for the CMF EOS, and for a $85M_{\odot}$ progenitor, it is stronger, appears earlier and lies at lower frequencies for the CMF EOS. The lower frequency

indicates a softening of the inner boundary of the PNS convection zone primarily due to a higher sound speed of the CMF EOS at densities of about $2 \times \rho_0$. The strength of PNS convection as a driver of the 2g_1 mode is sensitive to the EOS, which explains the stronger GW signal from this mode for the CMF EOS.

These results suggest that the supernova GW signal holds more promise for probing properties of nuclear matter beyond saturation density than hitherto thought because the signal from the ${}^{2}g_{1}$ mode is determined by the behavior of the EOS around $2 \times \rho_0$, in contrast to the dominant f/gmode, which lives primarily at the PNS surface and is determined by bulk PNS parameters. The use of the 2g_1 mode as a probe for the high-density EOS is not limited to the scenario of a first-order phase transition considered in earlier work [74–76]. The signal from the 2g_1 mode still cannot probe quark formation directly, but may be used to measure the stiffness of the EOS in the aforementioned density regime, which will have implications for the viability of a phase transition or smooth crossover to quark matter. Observations of the 2g_1 mode feature from a Galactic supernova could thus complement heavy-ion collisions [77] and current astrophysical constraints on the stiffness of the high-density EOS from pulsar masses [78] and NICER data [79,80] and the GW signal from neutron star mergers. The tidal deformability parameter from the premerger GW signal from GW170817 already rules out very stiff EOS [81,82]. In contrast, recent radius measurements by NICER argue against substantial softening of matter between $(2-3) \times \rho_0$ and $(4-5) \times \rho_0$ (that would accompany a strong first-order phase transition in this density regime) [83]. Future work should explore the impact of the EOS and of dimensionality on mode excitation and the signal from the ${}^{2}g_{1}$ mode more broadly. Encouragingly, despite generally lower GW amplitudes in three dimensions (3D), the signal has been found in 3D models after submission of our Letter [25]. One should also further clarify the physical parameters that govern the mode frequency and power and assess the potential of current and next-generation GW interferometers to detect the signal and reconstruct the trajectory of the mode frequency.

The authors are supported by the Australian Research Council (ARC) Centre of Excellence (CoE) for Gravitational Wave Discovery (OzGrav) project No. CE170100004. B. M. is supported by ARC Future Fellowship FT160100035. A. H. is supported by the ARC CoE for All Sky Astrophysics in 3 Dimensions (ASTRO 3D), through project number CE170100013. J. P. is supported by the ARC Discovery Early Career Researcher Award (DECRA) project No. DE210101050. A.M. acknowledges the Stern-Gerlach Postdoctoral fellowship and the educator program of the Stiftung Polytechnische Gesellschaft. H. S. thanks the Walter Greiner Gesellschaft zur Förderung der physikalischen Grundlagenforschung e.V. through the Judah M. Eisenberg Laureatus Chair at the Goethe Universität Frankfurt am Main. We acknowledge computer time allocations from Astronomy Australia Limited's ASTAC scheme, the National Computational Merit Allocation Scheme (NCMAS), and from an Australasian Leadership Computing Grant. Some of this work was performed on the Gadi supercomputer with the assistance of resources and services from the National Computational Infrastructure (NCI), which is supported by the Australian Government. Some of this work was performed on the OzSTAR national facility at Swinburne University of Technology. OzSTAR is funded by Swinburne University of Technology and the National Collaborative Research Infrastructure Strategy (NCRIS). Some of the computational resources were provided by the Goethe-HLR computing center. S. Z. is supported by the National Natural Science Foundation of China (Grant No. 12288102) and the International Centre of Supernovae, Yunnan Key Laboratory (No. 202302AN360001).

- *Corresponding author: pia.jakobus@monash.edu
- [1] The LIGO Scientific Collaboration, Classical Quantum Gravity **32**, 074001 (2015).
- [2] F. Acernese, M. Agathos, K. Agatsuma, D. Aisa, N. Allemandou, A. Allocca *et al.*, Classical Quantum Gravity 32, 024001 (2015).
- [3] H. Abe, T. Akutsu, M. Ando, A. Araya, N. Aritomi, H. Asada *et al.*, Galaxies **10**, 63 (2022).
- [4] B. P. Abbott, R. Abbott, T. D. Abbott, S. Abraham, F. Acernese, Ackley *et al.*, Phys. Rev. D **101**, 084002 (2020).
- [5] V. Kalogera, M.-A. Bizouard, A. Burrows, T. Janka, K. Kotake, Messer et al., BAAS 51, 239 (2019).
- [6] K. Hayama, T. Kuroda, K. Kotake, and T. Takiwaki, Phys. Rev. D 92, 122001 (2015).
- [7] M. J. Szczepańczyk, J. M. Antelis, M. Benjamin, M. Cavaglià, D. Gondek-Rosińska, T. Hansen *et al.*, Phys. Rev. D **104**, 102002 (2021).
- [8] M. Punturo, M. Abernathy, F. Acernese, B. Allen, N. Andersson, Arun *et al.*, Classical Quantum Gravity 27, 194002 (2010).
- [9] M. Szczepańczyk and M. Zanolin, Galaxies 10, 70 (2022).
- [10] J. Powell and B. Müller, Mon. Not. R. Astron. Soc. 487, 1178 (2019).
- [11] V. Srivastava, S. Ballmer, D. A. Brown, C. Afle, A. Burrows, D. Radice, and D. Vartanyan, Phys. Rev. D 100, 043026 (2019).
- [12] W. Li, R. Chornock, J. Leaman, A. V. Filippenko, D. Poznanski, X. Wang, M. Ganeshalingam, and F. Mannucci, Mon. Not. R. Astron. Soc. 412, 1473 (2011).
- [13] S. M. Adams, C. S. Kochanek, J. F. Beacom, M. R. Vagins, and K. Z. Stanek, Astrophys. J. 778, 164 (2013).
- [14] J. W. Murphy, C. D. Ott, and A. Burrows, Astrophys. J. 707, 1173 (2009).
- [15] B. Müller, H.-T. Janka, and A. Marek, Astrophys. J. 766, 43 (2013).
- [16] T. Kuroda, T. Takiwaki, and K. Kotake, Phys. Rev. D 89, 044011 (2014).

- [17] T. Kuroda, K. Kotake, and T. Takiwaki, Astrophys. J. Lett. 829, L14 (2016).
- [18] H. Andresen, B. Müller, E. Müller, and H. T. Janka, Mon. Not. R. Astron. Soc. 468, 2032 (2017).
- [19] K. N. Yakunin, A. Mezzacappa, P. Marronetti, E. J. Lentz, Bruenn *et al.*, arXiv:1701.07325.
- [20] T. Takiwaki and K. Kotake, Mon. Not. R. Astron. Soc. 475, L91 (2018).
- [21] V. Morozova, D. Radice, A. Burrows, and D. Vartanyan, Astrophys. J. 861, 10 (2018).
- [22] H. Andresen, E. Müller, H. T. Janka, A. Summa, K. Gill, and M. Zanolin, Mon. Not. R. Astron. Soc. 486, 2238 (2019).
- [23] D. Radice, V. Morozova, A. Burrows, D. Vartanyan, and H. Nagakura, Astrophys. J. Lett. 876, L9 (2019).
- [24] A. Mezzacappa, P. Marronetti, R. E. Landfield, E. J. Lentz, K. N. Yakunin, Bruenn *et al.*, Phys. Rev. D **102**, 023027 (2020).
- [25] D. Vartanyan, A. Burrows, T. Wang, M. S. B. Coleman, and C. J. White, Phys. Rev. D 107, 103015 (2023).
- [26] J. M. Blondin, A. Mezzacappa, and C. DeMarino, Astrophys. J. 584, 971 (2003).
- [27] H. Sotani, T. Kuroda, T. Takiwaki, and K. Kotake, Phys. Rev. D 96, 063005 (2017).
- [28] A. Torres-Forné, P. Cerdá-Durán, A. Passamonti, and J. A. Font, Mon. Not. R. Astron. Soc. 474, 5272 (2018).
- [29] A. Torres-Forné, P. Cerdá-Durán, A. Passamonti, M. Obergaulinger, and J. A. Font, Mon. Not. R. Astron. Soc. 482, 3967 (2019).
- [30] O. Eggenberger Andersen, S. Zha, A. da Silva Schneider, A. Betranhandy, S. M. Couch, and E. P. O'Connor, Astrophys. J. 923, 201 (2021).
- [31] A. Mezzacappa, P. Marronetti, R. E. Landfield, E. J. Lentz, W. R. Hix, J. A. Harris *et al.*, Phys. Rev. D **107**, 043008 (2023)
- [32] J. Powell and B. Müller, Phys. Rev. D 105, 063018 (2022).
- [33] C. Afle, S. K. Kundu, J. Cammerino, E. R. Coughlin, D. A. Brown, D. Vartanyan, and A. Burrows, Phys. Rev. D 107, 123005 (2023).
- [34] A. Torres-Forné, P. Cerdá-Durán, M. Obergaulinger, B. Müller, and J. A. Font, Phys. Rev. Lett. 123, 051102 (2019).
- [35] H. Sotani, T. Takiwaki, and H. Togashi, Phys. Rev. D 104, 123009 (2021).
- [36] N. A. Gentile, M. B. Aufderheide, G. J. Mathews, F. D. Swesty, and G. M. Fuller, Astrophys. J. 414, 701 (1993).
- [37] I. Bednarek, M. Biesiada, and R. Manka, arXiv:astro-ph/ 9608053.
- [38] I. Sagert, T. Fischer, M. Hempel, G. Pagliara, J. Schaffner-Bielich, A. Mezzacappa, F.-K. Thielemann, and M. Liebendörfer, Phys. Rev. Lett. 102, 081101 (2009).
- [39] T. Fischer, N.-U. F. Bastian, M.-R. Wu, P. Baklanov, E. Sorokina, S. Blinnikov, S. Typel, T. Klähn, and D. B. Blaschke, Nat. Astron. **2**, 980 (2018).
- [40] V. Dexheimer, L. T. T. Soethe, J. Roark, R. O. Gomes, S. O. Kepler, and S. Schramm, Int. J. Mod. Phys. E 27, 1830008 (2018).
- [41] E. R. Most, L. J. Papenfort, V. Dexheimer, M. Hanauske, S. Schramm, H. Stöcker, and L. Rezzolla, Phys. Rev. Lett. **122**, 061101 (2019).

- [42] A. Bauswein, N.-U. F. Bastian, D. B. Blaschke, K. Chatziioannou, J. A. Clark, T. Fischer, and M. Oertel, Phys. Rev. Lett. **122**, 061102 (2019).
- [43] M. Hanauske, L. Bovard, E. Most, J. Papenfort, J. Steinheimer, A. Motornenko, V. Vovchenko, V. Dexheimer, S. Schramm, and H. Stöcker, Universe 5, 156 (2019).
- [44] N. Yasutake, K. Kotake, M.-A. Hashimoto, and S. Yamada, Phys. Rev. D 75, 084012 (2007).
- [45] S. Zha, E. P. O'Connor, M.-c. Chu, L.-M. Lin, and S. M. Couch, Phys. Rev. Lett. 125, 051102 (2020).
- [46] T. Kuroda, T. Fischer, T. Takiwaki, and K. Kotake, Astrophys. J. 924, 38 (2022).
- [47] A. W. Steiner, M. Hempel, and T. Fischer, Astrophys. J. **774**, 17 (2013).
- [48] A. Motornenko, J. Steinheimer, V. Vovchenko, S. Schramm, and H. Stoecker, Phys. Rev. C 101, 034904 (2020).
- [49] B. Müller, H.-T. Janka, and H. Dimmelmeier, Astrophys. J. Suppl. Ser. 189, 104 (2010).
- [50] B. Müller and H. T. Janka, Mon. Not. R. Astron. Soc. 448, 2141 (2015).
- [51] L. S. Finn, in *Frontiers in Numerical Relativity*, edited by C. R. Evans, L. S. Finn, and D. W. Hobill (1989) pp. 126–145.
- [52] T. A. Weaver, G. B. Zimmerman, and S. E. Woosley, Astrophys. J. 225, 1021 (1978).
- [53] A. Heger and S. E. Woosley, Astrophys. J. **724**, 341 (2010).
- [54] E. R. Most, A. Motornenko, J. Steinheimer, V. Dexheimer, M. Hanauske, L. Rezzolla, and H. Stoecker, Phys. Rev. D 107, 043034 (2023).
- [55] P. Jakobus, B. Müller, A. Heger, A. Motornenko, J. Steinheimer, and H. Stoecker, Mon. Not. R. Astron. Soc. **516**, 2554 (2022).
- [56] J. Morlet, G. Arens, I. Forgeau, and D. Giard, Geophysics 47, 203 (1982).
- [57] A. Marek, H. T. Janka, and E. Müller, Astron. Astrophys. 496, 475 (2009).
- [58] K. N. Yakunin, P. Marronetti, A. Mezzacappa, S. W. Bruenn, C.-T. Lee, Chertkow *et al.*, Classical Quantum Gravity **27**, 194005 (2010).
- [59] P. Cerdá-Durán, N. DeBrye, M. A. Aloy, J. A. Font, and M. Obergaulinger, Astrophys. J. Lett. 779, L18 (2013).
- [60] H. Kawahara, T. Kuroda, T. Takiwaki, K. Hayama, and K. Kotake, Astrophys. J. 867, 126 (2018).
- [61] D. E. Myers, WIT Trans. Model. Simulation 23, 10 (1970).
- [62] S. Altiparmak, C. Ecker, and L. Rezzolla, Astrophys. J. Lett. **939**, L34 (2022).
- [63] Y. Fujimoto, K. Fukushima, and K. Murase, Phys. Rev. D 101, 054016 (2020).
- [64] S. Soma, L. Wang, S. Shi, H. Stöcker, and K. Zhou, Phys. Rev. D 107, 083028 (2023).
- [65] M. Omana Kuttan, J. Steinheimer, K. Zhou, and H. Stoecker, arXiv:2211.11670.
- [66] D. Oliinychenko, A. Sorensen, V. Koch, and L. McLerran, Phys. Rev. C 108, 034908 (2023).
- [67] See Supplemental Material at http://link.aps.org/supplemental/10.1103/PhysRevLett.131.191201 for the time evolution of the electron fraction gradient.
- [68] H. Nagakura, A. Burrows, D. Radice, and D. Vartanyan, Mon. Not. R. Astron. Soc. 492, 5764 (2020).

- [69] S. W. Bruenn and T. Dineva, Astrophys. J. Lett. 458, L71 (1996).
- [70] S. W. Bruenn, E. A. Raley, and A. Mezzacappa, arXiv:astro-ph/0404099.
- [71] R. Glas, H. T. Janka, T. Melson, G. Stockinger, and O. Just, Astrophys. J. 881, 36 (2019).
- [72] B. Müller, Liv. Rev. Comput. Astrophys. 6, 3 (2020).
- [73] L. F. Roberts, G. Shen, V. Cirigliano, J. A. Pons, S. Reddy, and S. E. Woosley, Phys. Rev. Lett. 108, 061103 (2012).
- [74] P. N. McDermott, Mon. Not. R. Astron. Soc. 245, 508 (1990).
- [75] T. E. Strohmayer, Astrophys. J. 417, 273 (1993).
- [76] G. Miniutti, J. A. Pons, E. Berti, L. Gualtieri, and V. Ferrari, Mon. Not. R. Astron. Soc. 338, 389 (2003).
- [77] S. Huth, P. T. H. Pang, I. Tews, T. Dietrich, A. Le Fèvre, A. Schwenk, W. Trautmann, K. Agarwal, M. Bulla, M. W. Coughlin, and C. Van Den Broeck, Nature (London) 606, 276 (2022).

- [78] P. B. Demorest, T. Pennucci, S. M. Ransom, M. S. E. Roberts, and J. W. T. Hessels, Nature (London) 467, 1081 (2010).
- [79] T. E. Riley, A. L. Watts, P. S. Ray, S. Bogdanov, S. Guillot, Morsink et al., Astrophys. J. Lett. 918, L27 (2021).
- [80] M. C. Miller, F. K. Lamb, A. J. Dittmann, S. Bogdanov, Z. Arzoumanian, Gendreau et al., Astrophys. J. Lett. 918, L28 (2021).
- [81] B. P. Abbott *et al.* (LIGO Scientific and Virgo Collaborations), Phys. Rev. Lett. 116, 061102 (2016).
- [82] B. P. Abbott, R. Abbott, T. D. Abbott, F. Acernese, K. Ackley, C. Adams *et al.* (The LIGO Scientific and the Virgo Collaborations), Phys. Rev. Lett. **121**, 161101 (2018).
- [83] T. Kojo, G. Baym, and T. Hatsuda, Astrophys. J. **934**, 46 (2022).